Multiphoton microscopy for structure identification in human prostate and periprostatic tissue: implications in prostate cancer surgery

Ashutosh K. Tewari[1,*], **Maria M. Shevchuk**[2], **Joshua Sterling**[3], **Sonal Grover**[1], **Michael Herman**[1], **Rajiv Yadav**[1], **Kumaran Mudalair**[1], **Abhishek Srivastava**[1], **Mark A. Rubin**[2], **Warren R. Zipfel**[4], **Frederick R. Maxfield**[3], **Chris Xu**[5], **Watt W. Webb**[5], and **Sushmita Mukherjee**[3,*]

[1]Prostate Cancer Institute and Lefrak Center of Robotic Surgery, Department of Urology, Weill Cornell Medical College, New York

[2]Department of Pathology and Laboratory Medicine, Weill Cornell Medical College, New York

[3]Department of Biochemistry, Weill Cornell Medical College, New York

[4]Department of Biomedical Engineering, Cornell University, Ithaca, NY, USA

[5]School of Applied and Engineering Physics, Cornell University, Ithaca, NY, USA

Abstract

- To test whether multiphoton microscopy (MPM) might allow identification of prostatic and periprostatic structures with magnification and resolution similar to gold standard histopathology.

- The present study included 95 robotic radical prostatectomy patients who consented to participate in an Institutional Review Board-approved study starting in 2007.

- The types of specimens used for imaging were excised surgical margins and biopsies, and sections obtained from the excised prostate.

- The specimens were imaged with a custom-built MPM system.

- All images were compared with haematoxylin/eosin histopathology of the same specimen.

- MPM of freshly excised, unprocessed and unstained tissue can identify all relevant prostatic and periprostatic structures, such as nerves, blood vessels, capsule, underlying acini and also pathological changes, including prostate cancer.

- Histological confirmation and correlation of these structures and pathologies have validated the findings of MPM.

- MPM shows great promise as a tool for real-time intra-surgical histopathology without needing excision or administration of contrast agents.

- The results will, however, need to be confirmed in true surgical settings using a miniaturized MPM microendoscope.

Correspondence: Dr Ashutosh K. Tewari, Department of Urology, Suite Starr 900, Weill Cornell Medical College, 525 East 68th Street, New York, NY 10065, USA (ashtewarimd@gmail.com); Dr Sushmita Mukherjee, Department of Biochemistry, Room E 00.02, Weill Cornell Medical College, 1300 York Ave., New York, NY 10065, USA (smukherj@med.cornell.edu).
*Drs Tewari and Mukherjee contributed equally to the study.

Keywords

robotic prostatectomy; multiphoton microscopy; prostate cancer; nerve sparing; histopathology; real-time imaging

Introduction

Prostate cancer is the most common male cancer, claiming almost 27 000 lives annually [1]. When confined to the gland, it can be successfully treated by surgical removal of the organ, a procedure termed radical prostatectomy, which is performed in 70 000 patients in the US every year. The success of this surgery is judged by three measures: complete removal of the cancer-harbouring glands; preservation of nerves that control sexual function; and preservation of sphincteric structures, which maintain urinary control.

Anatomically, the prostate gland is surrounded by a fibrous capsule, with a thickness that varies substantially between different parts of the gland. This incomplete capsule is surrounded, in turn, by a multi-layered, anatomically complex fascia that contains fat cells intermingled with loose areolar tissue, autonomic ganglia, a neural plexus, nerve trunks, arteries and veins. This fascia adheres to the capsule and is pierced by vessels and nerves. Both the erectile nerve, which has a variable branching pattern, and the sphincteric sling, are intermingled with the fascial fat, connective tissue and blood vessels [2].

Cancer cells sometimes migrate beyond the gland and either involve the surrounding nerves or grow into the sphincter – a phenomenon termed extra-prostatic extension (EPE). Since these nerves and any clusters of cancer cells are too small to be visualized by eye or using the ×10–12 magnification of the stereoscope of a surgical robot, the competing goals of cancer extirpation versus preservation of potency and continence have to be balanced during surgery [2]. Surgeons make judgments based on information that includes pre-surgical PSA levels, MRI results, DRE results and intra-surgical subjective cues such as colour changes, fibrosis and ease of separating the different fascial layers. One option for more detailed feedback, intraoperative frozen sections, takes time, could damage the delicate structures one is trying to save, and suffers from sampling errors. As a result, the current methods for discriminating between EPE and the tissues that need to be preserved during surgery are imprecise and have an impact on the outcomes of this surgery.

Indeed, this inability to identify cancerous cells and their association with nerves can result in incomplete removal of cancer, resulting in positive surgical margins (10–40% occurrence) [3–6], postoperative impotence due to damage to, or excision of, these nerves (25–70%) [7–11], or both positive margins and an impotent patient. It has been estimated that half the patients who undergo radical prostatectomy require postoperative treatment for erectile dysfunction. In addition to causing psychological and quality-of-life compromises, these complications exact a staggering financial cost on the US health care system. At a rate of US $10 000–20 000 per patient per year spent on doctors' office visits, oral medications, vacuum pumps, intra-cavernous injections and secondary surgeries, this costs the US health care system $350–700 million every year. In addition, certain patients are excluded as candidates for nerve-sparing surgery based on the less-than-optimal preoperative assessments, and thus could be denied a chance for a better postoperative quality of life.

In summary, access to high-resolution, high-contrast live imaging of the prostatic capsule, apex, sphincter and the surrounding nerves and tissues would improve surgical decision-making and patient outcomes, and reduce the emotional and financial impact of post-surgical complications.

One potential solution is a novel non-linear optical imaging technology: multiphoton microscopy (MPM) [12–14]. MPM relies on the simultaneous absorption of two (or three) low-energy (near-infrared) photons to cause a non-linear excitation, which greatly reduces the potential for cellular damage. Excitation only occurs where there is sufficient photon density (at the point of laser focus), providing intrinsic optical sectioning with a resolution equivalent to traditional confocal microscopy. Tissue penetration is greater than standard confocal microscopy because absorption and scattering are greatly reduced at near-infrared wavelengths compared with the visible or ultraviolet spectrum.

Most importantly, by utilizing two-photon excitation in the 700–800 nm range, MPM enables the imaging of fresh, living, unprocessed and unstained tissue by utilizing intrinsic tissue emissions (ITEs). The ITE signal is composed of two components: tissue autofluorescence, in part from nicotinamide adenine dinucleotide (NADH) and flavin adenine dinucleotide (FAD) in cells, elastin in the connective tissue, and lipofuscin in fat and other cells; and second harmonic generation (SHG), which arises from non-centrosymmetric structures such as tissue collagen [12–14]. We and others have shown that MPM/ITE imaging is capable of generating distinctive optical signals that enable imaging of animal [13] and human [15–17] tissues at sub-micron resolution in three dimensions to a depth of up to 0.5 mm; at image acquisition rates of $\approx$ one image/second, with $>10^5$ pixels per image.

While the miniaturization of MPM for integration with robotic surgical equipment is currently in progress, we have carried out a prospective study to assess the feasibility of using MPM/ITE for structure identification in excised prostatic and periprostatic tissue. In all cases, the MPM findings were confirmed by comparison with gold standard haematoxylin/eosin (H&E)-stained histopathology.

Specimens were obtained from consenting subjects undergoing robotic radical prostatectomy at Weill Cornell Medical College with Dr Tewari, in a protocol approved by the Institutional Review Board. Samples included periprostatic tissue, specifically surgical margins containing the lateral pelvic fascia (LPF), as well as the prostatic acini, in the form of either biopsies or sections of the gland. In LPF specimens, we confirm our ability to identify its components, such as nerves, arteries, fat and connective tissue, as well as sites of local inflammation. These structures are the ones that must be identified during surgery. In the excised specimens (biopsies or sections), we identify the prostatic acini, the surrounding stroma, and the prostatic capsule. Architectural changes in malignant transformation are used during histopathology to determine tumour grade (Gleason grade), and hence the aggressiveness, of the cancer. We show here that MPM/ITE can provide such architectural information.

Material and Methods

The present study included 95 robotic radical prostatectomy patients who agreed to participate in an Institutional Review Board-approved study starting in 2007.

Two types of specimens were used for MPM imaging: excised surgical margins and biopsies; and sections obtained from the excised prostate. The former specimens were brought to the multiphoton facility immediately after excision. In the latter case, prostates removed by radical prostatectomy were taken immediately to the Department of Surgical Pathology, where the specimen surfaces were inked as per institutional protocol, and then the specimen was sliced in roughly 0.5-cm sections. Sections chosen by a urology fellow with the assistance of a uropathologist, based on expected pathology, were then brought to

the multiphoton facility. In either case, the tissue specimens were placed in normal saline on ice for transport, and imaged at room temperature with a MPM.

If necessary, the specimen was stabilized at the best orientation using non-toxic modelling clay, and a coverslip was placed on top to avoid adhesion of the specimen to the water immersion objective due to capillary action. Once oriented, the specimen was imaged using a custom-built MPM imaging system consisting of an Olympus BX61 upright microscope (Olympus America Inc., Center Valley, PA, USA) and a modified Bio-Rad 1024 scanhead (Bio-Rad Laboratories, Hercules, CA, USA) with near-infrared optics and a three-channel external detection system. The specimens were excited using a tunable Ti-Sapphire laser (Mai Tai HP, Spectra-Physics Lasers, Newport Corp., Irvine, CA, USA), tuned to 780 nm. The laser intensity control and fly-back blanking were provided by a Pockels Cell (Model 350-80 LABK, Conoptics Inc., Danbury, CT, USA), and consistently kept at or below 60–80 mW in the sample plane. No substantial tissue damage was observed either during imaging or in the histopathology slides later prepared from the imaged specimens.

Images were collected in either two or three channels (each channel used a blue sensitive Bialkali photomultiplier tube: Model R1924, Hamamatsu Photonics, Bridgewater, NJ). For two-channel imaging, the signals collected were as follows: an SHG signal centred at 390 nm ($\pm$ 35 nm); and a short-wavelength autofluorescence between 420 and 530 nm. In the case of three-channel detection, the first two channels were identical to the ones described earlier, and an additional detector was used to collect long-wavelength autofluorescence (530–650 nm).

Images were acquired at several magnifications: low magnification for obtaining overall architectural information [$\times$4, 0.28 numerical aperture (NA) dry objective, imaging 3 mm^2 frames at 6 μm/pixel resolution]; intermediate magnification ($\times$10, 0.4 NA dry objective, imaging 1228 μm^2 frames at 2.4 μm/pixel resolution); and high magnification for obtaining detailed cellular and local architectural information ($\times$20, 0.95 NA water-immersion objective, imaging 614 μm^2 frames at 1.2 μm/pixel resolution). Higher digital zooms were used to increase magnification, if necessary. When imaging with the $\times$20 water immersion objective, a drop of normal saline was placed on the coverslip to achieve water immersion. All images were obtained as stacks of optical sections that extended through the entire depth of the specimen that produced reasonable signal. All image acquisition was carried out with LaserSharp 2000 software from Bio-Rad.

Greyscale images from LaserSharp 2000 were transferred to MetaMorph v7.0r4 (Molecular Devices, Sunnyvale, CA, USA), where they were colour-coded and merged. They were processed minimally (adjustment of brightness and contrast, Gaussian filtering to remove single pixel noise, placement of scale bars and cropping, if appropriate) using Adobe Photoshop CS3 (San Jose, CA, USA).

For all specimens, MPM/ITE imaging time was kept under an hour, at which time the specimen was returned to the Department of Surgical Pathology. For excised surgical margins and biopsies, the specimens were processed for routine histopathology (formalin fixation, embedding, sectioning and staining). Sections obtained from the excised prostate were immediately frozen and a portion sectioned further to prepare H&E-stained slides. The rest of the specimen was kept frozen and, after clinical diagnosis, was released to the prostate cancer tissue bank. This section is banked frozen and is available for further analysis in the future.

All slides from H&E staining were compared with the corresponding MPM images by genitourinary pathologists (MAR, MMS). In some cases, we enhanced our structure identification by using specific stains, such as Weigert's stain to identify elastin.

Results

Identification of relevant features in the periprostatic space and on the prostate surface

The human prostate is surrounded by a multi-layered fascial covering, which is composed of collagen, fat and smooth muscle. Vessels (both arteries and veins) of varying size and nerves and ganglion cells are interposed between the capsule and fascial layer. In Figure 1A, we show a low-magnification MPM image of a region of surgically excised LPF; Figure 1B shows an image from a histopathology slide prepared from the same specimen. At this low magnification, salient histological features (a, artery; b, loose connective tissue; and c, fat) are clearly visible. Figures 1C and 1D show low-magnification images of the lateral pelvic fascia with a coiled nerve and an artery, respectively (arrows). Note that the lumen of the artery (dark, non-fluorescent central space) is clearly visible in the optical section shown in Figure 1D. This enables arteries to be distinguished from nerves, as the latter do not have a lumen. Figure 1C also shows clearly distinguishable signals from collagen (SHG, red; small arrowhead) and elastin (autofluorescence, green; large arrowhead) in the connective tissue. Figures 1E and 1F show a nerve and two arteries, respectively, at a higher magnification. Note the wavy pattern of the nerve fibres in Figure 1E, and the three layers of the arterial wall (ti, tunica intima; tm, tunica media; ta, tunica adventitia), clearly seen in cross-section in Figure 1F. Tunica intima has a high content of elastin (elastica interna), and thus is visible at longer, autofluorescent wavelengths (coded green), whereas the adventitia has more collagen, and thus has higher SHG signal (coded red). Figure 1G shows that MPM can be used to trace a small nerve through several lateral and vertical planes, something that will be essential for identifying a longitudinal structure during surgery. Figure 1H shows a relatively high magnification image of a surgical specimen encompassing a peripheral zone acinus (a), the parallel longitudinal collagen-rich fibres of the prostatic capsule (b), and the very proximal fascia containing collagen-rich connective tissue (c) and fat (d). Thus, MPM/ITE imaging enables detection of microscopic details that allow accurate recognition of surgically relevant tissues present in the prostatic fascia, something that is not possible with current surgical technology.

Documentation of the intraprostatic architecture

The prostate gland is composed of acini, which are dispersed in the fibromuscular stroma of the gland. The stroma generates strong SHG signal due to the abundance of collagen, whereas the acini are strongly autofluorescent. Each acinus consists of a double layer of cells lining a central lumen. This organisation is shown in Figures 2A and 2C (low and high magnification). Figures 2B and 2D show the corresponding images from slides stained with H&E. The acini often contain strongly autofluorescent concretions (arrows in Fig. 1A). At higher magnification, one sees prominent lumina in the prostatic acini (Figs 2C, 2D).

When imaged using MPM, prostatic acini show strong punctate autofluorescence. Although the punctae appear to be cell-associated, they do not exhibit a true cellular morphology (i.e. dark nuclei surrounded by an autofluorescent cytoplasm), such as those seen in the MPM/ITE images of bladder urothelium [15] or gastrointestinal epithelium [16].

In Figures 2E, 2G and 2H, we show that this punctate autofluorescence has spectroscopic properties distinct from the elastin fluorescence observed in the intima of neighbouring arteries, or cytoplasm-derived autofluorescence observed in cells. This difference can be clearly appreciated in Figure 2E, where the structure marked 'a' shows a prostatic acinus, while that marked 'b' shows elastin in the artery wall. This difference arises because elastin autofluorescence is mostly observed in our lower-wavelength autofluorescence detection channel (420–530 nm; colour-coded green), whereas the punctuate acinar signal is present in both the low- and high-wavelength autofluorescence detection channels (the higher-

wavelength autofluorescence channel collects emissions in the 530–650 nm range and is colour-coded blue). Thus, the punctuate autofluorescence appears cyan to blue in our colour-coding scheme, depending on the relative contributions from the two autofluorescence detection channels.

Similarly, this punctate autofluorescence is distinct from the autofluorescence arising from cell cytoplasm at higher magnification (Figs 2G, 2H). Cellular autofluorescence mainly originates from intracellular NADH and FAD [12–14], and cells typically have much more NADH than FAD. NADH emission is mostly restricted between 420 and 530 nm, and thus cell cytoplasms appear green in our colour-coding scheme. Bona fide cells with green fluorescent cytoplasm surrounding dark nuclei are shown with arrows in Figures 2G and 2H. While the source of the long-wavelength-emitting punctate autofluorescence in prostatic acini is not established, we hypothesize that it arises from lipofuscin deposits in the lysosomes of the prostatic acinar cells [18–21].

These data show that normal prostatic structures and cells, as well as the fibrocollagenous stroma, can be identified using MPM/ITE imaging. Recognition of these details is essential for decisions regarding the surgical plane used during radical prostatectomy to minimize positive margin rates.

Identification of intraprostatic and periprostatic alterations, including benign and malignant lesions

In Figure 3, we show the ability of MPM/ITE to identify various benign and malignant tissues in the prostate. Figure 3A shows a gland with prostatic epithelial hyperplasia, where there are many layers of autofluorescent prostatic cells that largely fill the lumen of the gland. Figure 3B shows an image from an H&E-stained slide prepared from the same specimen.

Gleason score, the primary method of grading prostate cancer, is based on glandular architecture [22, 23]. Thus, even at low magnification, it is possible to obtain useful data. Figure 3C shows a region from a prostate specimen with a low-grade tumour (Gleason grade 3) composed of many small glands. Figure 3D shows H&E-stained histopathology from a similar area of the same sample; similar features can be identified in both images. Figure 3E shows a section of the prostate from a subject with high-grade tumour [Gleason 7 (3+4)]. The region marked 'a' shows tumour with Gleason grade 3 (small, delineated glands), while the region marked 'b' shows Gleason grade 4 (sheets of cells with no apparent glandular organization). Figure 3F shows an H&E-stained section from the same specimen, showing the corresponding areas with Gleason grade 3 and 4 tumours marked 'a' and 'b', respectively.

Figure 3H shows a section of the LPF with a lymphoid aggregate, indicative of inflammation at that site. Inflammation is quite common, and could represent a site of recent biopsy, and the indurations resulting from it could falsely suggest a cluster of prostatic cells that have escaped into the periprostatic space (EPE). In the MPM/ITE image, we can see the lymphoid aggregate (a), surrounding arteries (b–d), and fat (e) in the fascia. Figure 3I shows a higher-magnification image of the lymphoid aggregate, in which individual lymphatic cells are clearly visible. Figure 3G shows an H&E-stained section from the specimen showing the corresponding structures, which are identified as in Figure 3H.

We conclude that MPM/ITE can be used to identify pathologies, obtain cancer grading information and identify sites of inflammation. Most importantly, it provides the ability to discriminate between pathologies and benign inflammation, something that can enable more accurate decisions regarding tissue removal.

Identification of extraprostatic structures that lie in the vicinity of the prostate

In Figure 4, we show the ability of MPM/ITE to image extraprostatic structures that are encountered routinely in the surgical context. Figures 4A and 4B show MPM/ITE images of a cross-section of the seminal vesicle at two different magnifications. The highly folded glands of the seminal vesicle (a) are clearly visible, surrounded by the convoluted stroma, consisting of loose connective tissue (b). A small portion of the fibromuscular wall is seen in both Figure 4A (labelled c) and the H&E image (Figure 4C, region c). The cyan-to-blue punctate autofluorescence in the seminal vesicle glands possibly originate from lipofuscin, as discussed earlier. The folded stroma appears to contain elastin and/or smooth muscle, based on signal in the autofluorescence channel (green) and collagen (the SHG channel; coded red). Consequently, these mucosal folds appear yellow due to the overlap of red and green signal. Figure 4C shows a corresponding area from an H&E-stained histopathology section.

Figures 4E and 4F show MPM/ITE images of a section of the vas deferens at two magnifications. This tissue has a much thicker fibromuscular wall (labelled c in all panels), and a smaller lumen with a less convoluted epithelium (a) and the loose connective tissue mucosa (b), compared with the seminal vesicle. Figure 4D shows a corresponding area from an H&E-stained histopathology section, identifying the same histological landmarks. Thus, MPM/ITE is capable of aiding in the identification of the vas deferens and seminal vesicles, tissues neighbouring the prostate, which are frequently invaded by cancerous prostate cells.

Discussion

In the present study, we show that MPM/ITE imaging generates high-resolution, high-contrast images from fresh, unprocessed and unstained tissue based solely on ITE (autofluorescence and SHG) signatures. The anatomical details that can be seen in these images make it an ideal candidate to assist in a surgical decision-making process during nerve-sparing radical prostatectomy.

Previous studies indicate that MPM is effective and safe. It has been used for nerve visualizations both *ex vivo* [24] and *in vivo* [25, 26], and has been reported to successfully image pathologies associated with Alzheimer's [25] and Parkinson's diseases [27] in transgenic mouse models. Recently, we have utilized MPM/ITE for real time *ex vivo* imaging of the prostate and periprostatic neuronal tissue in Sprague–Dawley rats, and obtained high-resolution images with minimal phototoxic effect on tissues [17].

The capabilities of MPM imaging have the potential to reduce the challenges of successful prostatectomy, which requires rapid identification of cancerous cells, the prostatic capsule and nerve bundles. The ability of MPM to produce optically thick image stacks is crucial, as visualization of the tissue underneath the visible surface could provide important information about the region of interest without requiring excision and conventional histopathology. We are currently working on developing a tool for integration of MPM/ITE and other pre-surgical and intra-surgical imaging methods. We expect that such a tool will help reduce positive margin rates, enhance surgeons' ability to identify and spare important nerves, and avoid damage to surrounding tissues.

It is fair to expect that MPM imaging will have to overcome several potential challenges before it can be integrated into surgical procedures. For example, it is possible that the overall cost of equipment, surgical suite adjustments and additional training of surgeons could render this technology too expensive for translation. We could also find that the actual surgical field contains more challenges, such as blood and fatty deposits that might interfere with the signal. Breathing and other types of ambient motions might also limit the quality of

the images, as current image acquisition rates are relatively slow (≈ one frame/s for a single plane). However, new technologies in this field are being developed at a rapid pace (e.g., cheaper, stable and portable single-wavelength femtosecond pulsed lasers, more efficient optical fibres, faster scan systems, adaptive optics to correct for aberrations, more efficient detectors and new optics that will increase the field of view while maintaining cellular resolution). It is thus very likely that, as challenges for clinical translation are identified, technological development will keep pace with addressing them.

In conclusion, we have utilized a novel approach for imaging of human prostatic and periprostatic tissue that can provide cellular-level information without any processing or exogenous contrast agents. Once technology to translate this imaging modality to the operating room becomes available, it should enable more accurate surgical decision-making. As discussed earlier, several technological challenges still remain to make this translation a reality; however, extensive research is continually generating newer solutions to the identified problems. We anticipate that the study presented here will lay the foundation for the development of methodologies applicable during surgery. We are currently pursuing further research in both human tissue and in small animal models to test the efficacy of this methodology in the surgical context.

Acknowledgments

References

1. Jemal A, Siegel R, Ward E, Murray T, Xu J, Thun MJ. Cancer statistics, 2007. CA Cancer J Clin. 2007; 57:43–66. [PubMed: 17237035]

2. Tewari A, Rao S, Martinez-Salamanca JI, Leung R, Ramanathan R, Mandhani A, Vaughan ED, Menon M, Horninger W, Tu J, et al. Cancer control and the preservation of neurovascular tissue: how to meet competing goals during robotic radical prostatectomy. BJU Int. 2008; 101:1013–1018. [PubMed: 18261153]

3. Smith RC, Partin AW, Epstein JI, Brendler CB. Extended followup of the influence of wide excision of the neurovascular bundle(s) on prognosis in men with clinically localized prostate cancer and extensive capsular perforation. J Urol. 1996; 156:454–457. discussion 457-458. [PubMed: 8683701]

4. Wieder JA, Soloway MS. Incidence, etiology, location, prevention and treatment of positive surgical margins after radical prostatectomy for prostate cancer. J Urol. 1998; 160:299–315. [PubMed: 9679867]

5. Watson RB, Civantos F, Soloway MS. Positive surgical margins with radical prostatectomy: detailed pathological analysis and prognosis. Urology. 1996; 48:80–90. [PubMed: 8693658]

6. Sofer M, Hamilton-Nelson KL, Schlesselman JJ, Soloway MS. Risk of positive margins and biochemical recurrence in relation to nerve-sparing radical prostatectomy. J Clin Oncol. 2002; 20:1853–1858. [PubMed: 11919244]

7. Bentas W, Wolfram M, Jones J, Brautigam R, Kramer W, Binder J. Robotic technology and the translation of open radical prostatectomy to laparoscopy: the early Frankfurt experience with robotic radical prostatectomy and one year follow-up. Eur Urol. 2003; 44:175–181. [PubMed: 12875935]

8. Ahlering TE, Skarecky D, Lee D, Clayman RV. Successful transfer of open surgical skills to a laparoscopic environment using a robotic interface: initial experience with laparoscopic radical prostatectomy. J Urol. 2003; 170:1738–1741. [PubMed: 14532766]

9. Eden CG, Cahill D, Vass JA, Adams TH, Dauleh MI. Laparoscopic radical prostatectomy: the initial UK series. BJU Int. 2002; 90:876–882. [PubMed: 12460349]

10. Rassweiler J, Marrero R, Hammady A, Erdogru T, Teber D, Frede T. Transperitoneal laparoscopic radical prostatectomy: ascending technique. J Endourol. 2004; 18:593–599. discussion 599-600. [PubMed: 15597643]

11. Saranchuk JW, Kattan MW, Elkin E, Touijer AK, Scardino PT, Eastham JA. Achieving optimal outcomes after radical prostatectomy. J Clin Oncol. 2005; 23:4146–4151. [PubMed: 15961762]

12. Denk W, Strickler JH, Webb WW. Two-photon laser scanning fluorescence microscopy. Science. 1990; 248:73–76. [PubMed: 2321027]

13. Zipfel WR, Williams RM, Christie R, Nikitin AY, Hyman BT, Webb WW. Live tissue intrinsic emission microscopy using multiphoton-excited native fluorescence and second harmonic generation. Proc Natl Acad Sci U S A. 2003; 100:7075–7080. [PubMed: 12756303]

14. Zipfel WR, Williams RM, Webb WW. Nonlinear magic: multiphoton microscopy in the biosciences. Nat Biotechnol. 2003; 21:1369–1377. [PubMed: 14595365]

15. Mukherjee S, Wysock JS, Ng CK, Akhtar M, Perner S, Lee MM, Rubin MA, Maxfield FR, Webb WW, Scherr DS. Human bladder cancer diagnosis using Multiphoton microscopy. Proc Soc Photo Opt Instrum Eng. 2009; 7161:nihpa96839. [PubMed: 19360140]

16. Rogart JN, Nagata J, Loeser CS, Roorda RD, Aslanian H, Robert ME, Zipfel WR, Nathanson MH. Multiphoton imaging can be used for microscopic examination of intact human gastrointestinal mucosa ex vivo. Clin Gastroenterol Hepatol. 2008; 6:95–101. [PubMed: 18065276]

17. Yadav R, Mukherjee S, Hermen M, Tan G, Maxfield FR, Webb WW, Tewari AK. Multiphoton microscopy of prostate and periprostatic neural tissue: a promising imaging technique for improving nerve-sparing prostatectomy. J Endourol. 2009; 23:861–867. [PubMed: 19425823]

18. Ablin RJ, Guinan P, Bush IM. Lipofuscin granules in normal, benign and malignant human prostatic tissue. Urol Res. 1973; 1:149–151. [PubMed: 4133104]

19. Amin MB, Bostwick DG. Pigment in prostatic epithelium and adenocarcinoma: a potential source of diagnostic confusion with seminal vesicular epithelium. Mod Pathol. 1996; 9:791–795. [PubMed: 8832564]

20. Brennick JB, O'Connell JX, Dickersin GR, Pilch BZ, Young RH. Lipofuscin pigmentation (so-called "melanosis") of the prostate. Am J Surg Pathol. 1994; 18:446–454. [PubMed: 7513501]

21. Mahmoodi M, Zhang S, Salim S, Hou JS, Garcia FU. Lipofuscin pigment can be used as a prognostic marker in prostatic adenocarcinoma. Ann Diagn Pathol. 2006; 10:257–262. [PubMed: 16979516]

22. Gleason DF. Classification of prostatic carcinomas. Cancer Chemother Rep. 1966; 50:125–128. [PubMed: 5948714]

23. Gleason DF, Mellinger GT. Prediction of prognosis for prostatic adenocarcinoma by combined histological grading and clinical staging. J Urol. 1974; 111:58–64. [PubMed: 4813554]

24. Dombeck DA, Kasischke KA, Vishwasrao HD, Ingelsson M, Hyman BT, Webb WW. Uniform polarity microtubule assemblies imaged in native brain tissue by second-harmonic generation microscopy. Proc Natl Acad Sci U S A. 2003; 100:7081–7086. [PubMed: 12766225]

25. Christie R, Bacskai B, Zipfel W, Williams R, Kajdasz S, Webb W, Hyman B. Growth arrest of individual senile plaques in a model of Alzheimer's disease observed by in vivo multiphoton microscopy. J Neurosci. 2001; 21:858–864. [PubMed: 11157072]

26. Levene MJ, Dombeck DA, Kasischke KA, Molloy RP, Webb WW. In vivo multiphoton microscopy of deep brain tissue. J Neurophysiol. 2004; 91:1908–1912. [PubMed: 14668300]

27. Day M, Wang Z, Ding J, An X, Ingham CA, Shering AF, Wokosin D, Ilijic E, Sun Z, Sampson AR, et al. Selective elimination of glutamatergic synapses on striatopallidal neurons in Parkinson disease models. Nat Neurosci. 2006; 9:251–259. [PubMed: 16415865]

Abbreviations

EPE   extra-prostatic extension

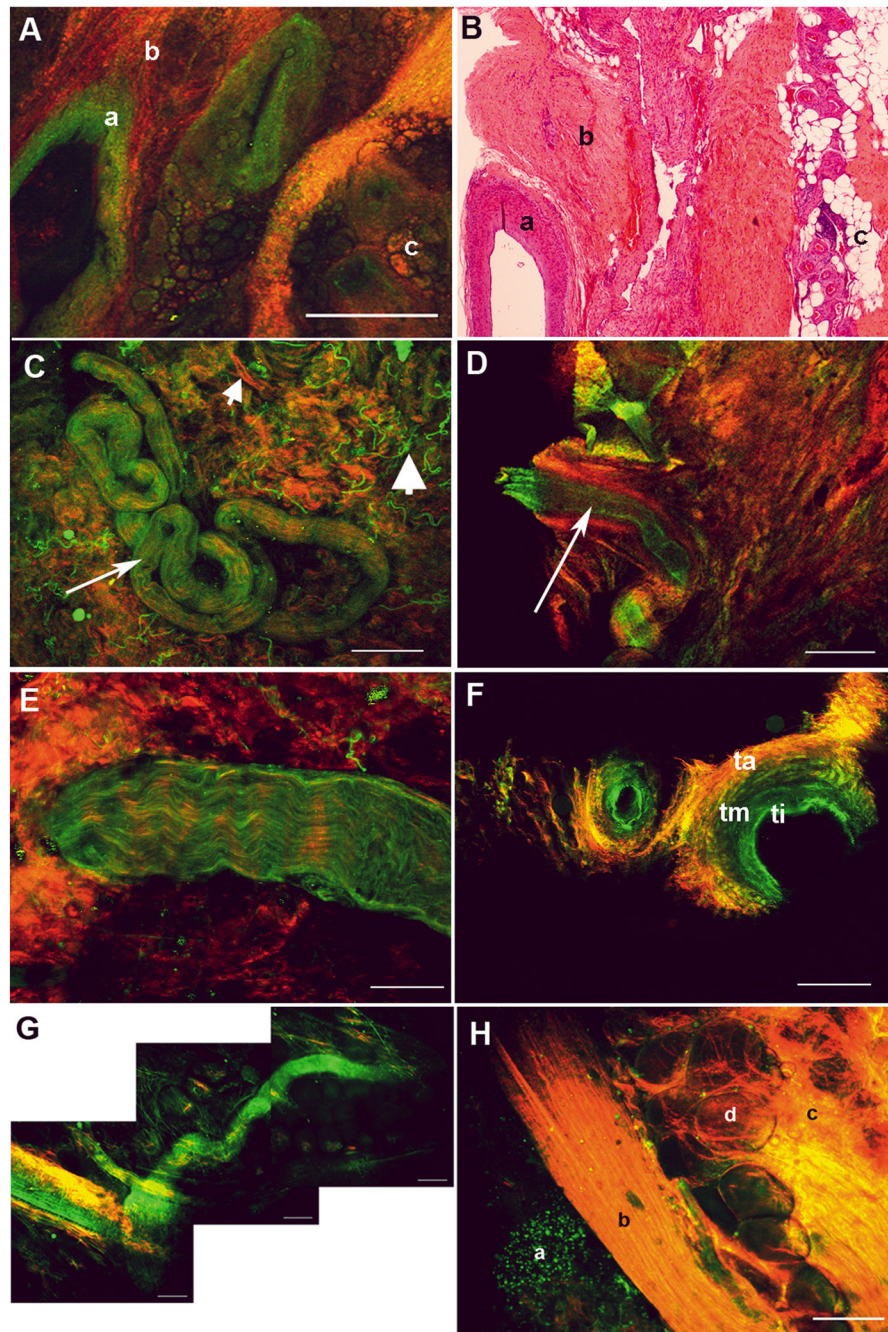| FAD | flavin adenine dinucleotide |
H&E	haematoxylin/eosin
ITE	intrinsic tissue emission
LPF	lateral pelvic fascia
MPM	multiphoton microscopy
NADH	nicotinamide adenine dinucleotide
SHG	second harmonic generation

FIG. 1.
MPM imaging of periprostatic fascia obtained from intra-surgical margins. (A, B) Lateral prostatic fascia showing a large artery (a), connective tissue (b) and fat (c). (A) MPM image. (B) Histology slide with Weigert's stain to identify elastin. (C) Surgical apical margin showing a small nerve (arrow). Small arrowhead points to collagen, large arrowhead to elastin, in the connective tissue. (D) Surgical apical margin showing a small artery (arrow; note the empty lumen as opposed to C). (E) Higher magnification image of a small nerve bundle at the surgical margin, showing fluorescence that derives from the axoplasm or the cytoplasm of the Schwann cells. (F) Higher magnification image of a small artery at the surgical margin, showing the elastin-rich tunica intima (ti; green), tunica media (tm) with

intermediate amount of elastin, and tunica adventitia (ta), which is rich in collagen. (G) A nerve bundle traced through several lateral and vertical planes. (H) Prostatic capsule showing an underlying acinus (a), the capsule (b), periprostatic fascial connective tissue (c) and fat (d). Colour-coding of all MPM images: red, SHG; green, autofluorescence between 420 and 530 nm. Scale bars: A, C, D, 500 μm; E, 67 μm; F, G, 200 μm; H, 100 μm.
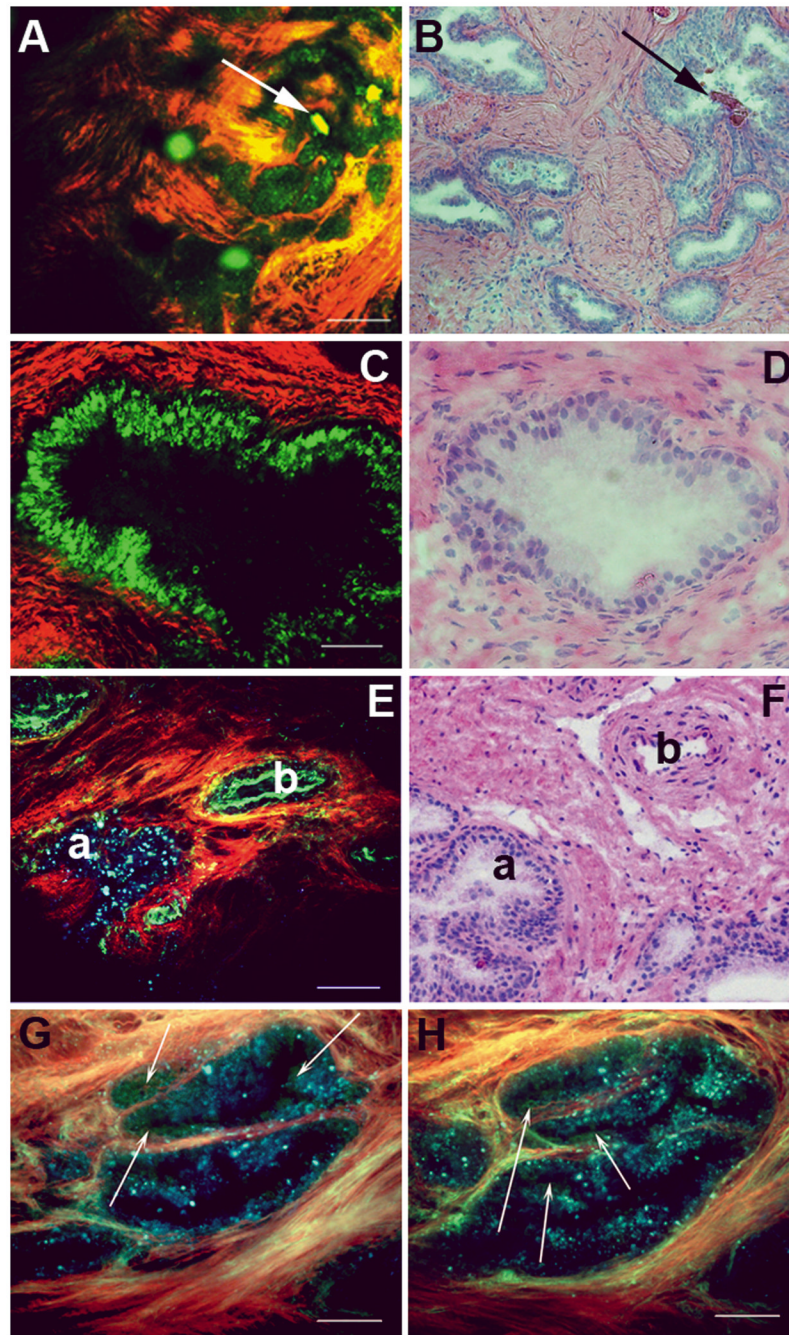
FIG. 2.
MPM and corresponding histology images of the prostate gland. (A, B) Low-magnification image of human prostate gland showing concretions. The MPM image (A) shows acini containing structures that are probably concretions (green; shown by arrows) and collagenous stroma (red). Panel B shows an H&E-stained sample from a corresponding area. (C, D) Higher-magnification view of prostatic glands. The MPM image (C) shows acinar cells (green) and collagenous stroma (red). Panel D shows image of H&E-stained sections from a corresponding area. (E, F) Prostatic acinus and nearby artery (on the capsule) showing differing autofluorescence signals. The prostate gland exhibits punctate fluorescence (a) over a very broad wavelength range (420–650 nm). By contrast, elastin

fluorescence in the artery (b) is predominantly restricted to the shorter wavelength channel (420–530 nm). Panel F shows H&E-stained sections from corresponding areas of the same specimen. (G, H) Higher magnification of prostatic acini imaged using three detector channels (two for autofluorescence; identical imaging conditions as in panel E). Here, cells emit mostly in the 420–530 nm range and thus appear green in the colour-coding scheme. By contrast, the gland-associated punctate fluorescence (which could represent lipofuscin deposits) emits over a broader wavelength range, and thus appears bluer in the colour-coding scheme (arrows point to bona fide cells with distinct nuclei). Colour-coding of MPM images: red, SHG (355–420 nm); green, short-wavelength autofluorescence (420–530 nm); blue, long-wavelength autofluorescence (530–650 nm). Scale bars: A, E, 200 μm; C, 50 μm; G, H, 100 μm.
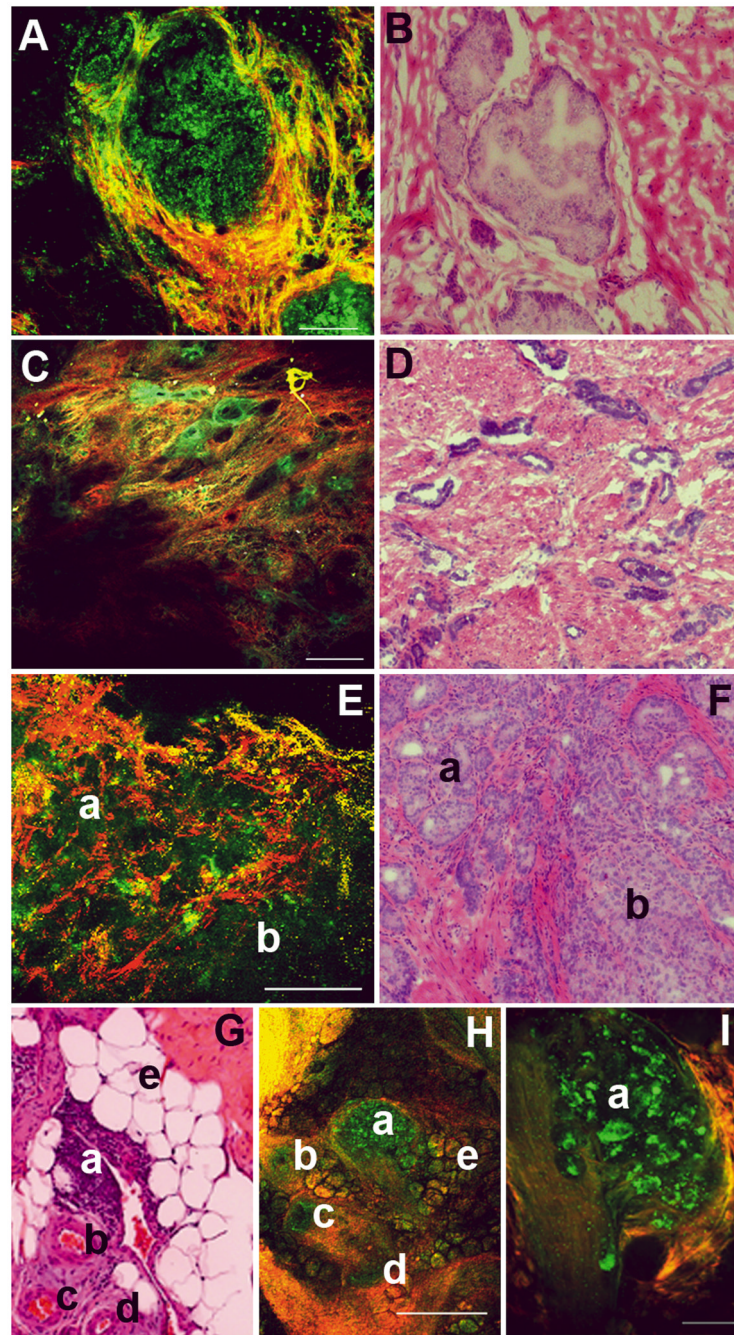
FIG. 3.
MPM and corresponding histopathology images of intraprostatic and periprostatic alterations, including benign and malignant lesions. (A, B) Prostatic epithelial hyperplasia. The MPM image (A) shows an acinus where the lumen is nearly filled with proliferating cells (autofluorescent). The acinus is demarcated by the presence of surrounding fibrocollagenous stroma. Panel B shows an H&E-stained sample from a corresponding area. (C, D) Panel C shows a low-magnification image of a malignant low-grade prostate cancer (Gleason grade 3), with small glands dispersed in the prominent fibrocollagenous stroma. Panel D shows H&E-stained image from a corresponding area. (E, F) Low-magnification images of human prostate gland showing high Gleason grade tumour. In the MPM image

(panel E), two regions can be identified: small glands can still be distinguished (a, Gleason grade 3) and sheets of fused glands with no glandular architecture or intervening stroma (b, Gleason grade 4). Panel F shows an H&E-stained image from a corresponding area. (G–I) Inflammatory pathology in the LPF. Panel H shows a low-magnification MPM image of a region of the fascia where we can identify a lymphoid aggregate (a), several arteries (b–d) and fat (e). Panel I shows a higher magnification of the lymphoid aggregate, with individual lymphocytes visible. Panel G shows an H&E-stained section of the corresponding area of the same specimen. Colour-coding of MPM images: A, C: red, SHG; green: autofluorescence between 420 and 530 nm. Scale bars: A, I, 100 μm; C, H, 500 μm; E, 200 μm.
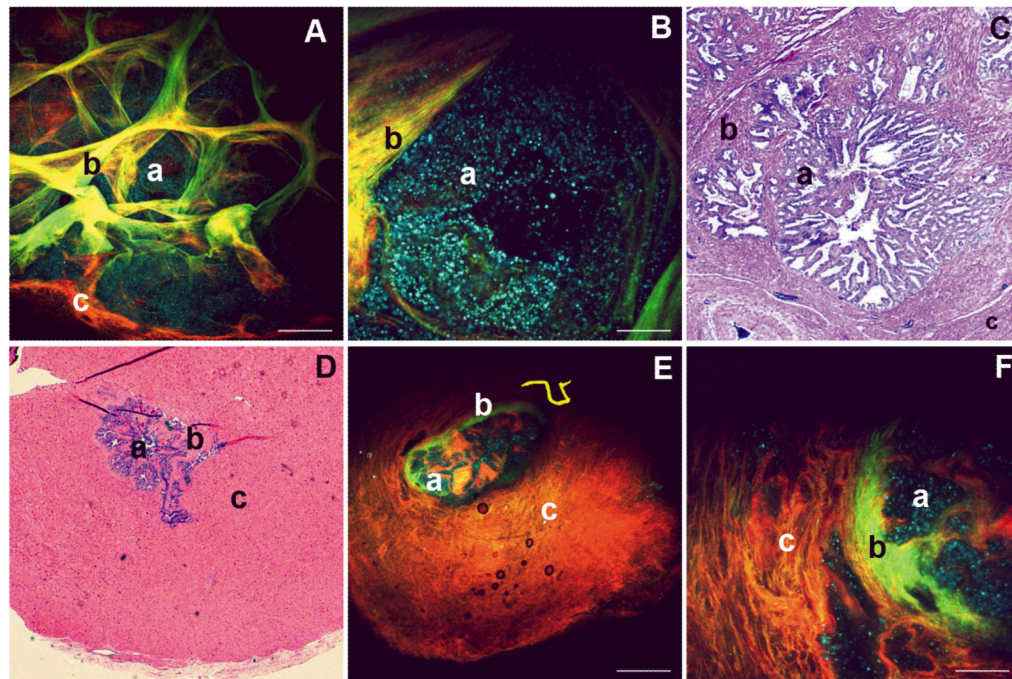
FIG. 4.
MPM and corresponding histopathology images of extraprostatic structures that are encountered during surgery. (A–C) Seminal vesicle. Panel A shows a low-magnification MPM image of a cross-section of the human seminal vesicle. A highly convoluted gland is visible (punctuate autofluorescence, colour-coded blue, possibly due to high levels of lipofuscin accumulation). The folds appear yellow, indicating these structures contain both autofluorescent components (elastin, smooth muscle cells) and structures that produce SHG signal (collagen). Panel B shows a higher magnification of a section of the gland. Panel C shows an image of an H&E-stained section prepared from the same specimen. (D–F) Vas deferens. Panel E shows a low-magnification MPM image of a cross-section of the vas deferens, showing a thick fibromuscular wall, a small lumen and a less convoluted glandular architecture than the seminal vesicle. Panel F shows a higher-magnification view of this region of the gland. Panel D shows an image of an H&E-stained section prepared from the same specimen. In all panels: a, gland; b, stroma consisting of loose connective tissue; c, fibromuscular wall. Colour-coding of MPM images: red, SHG (355–420 nm); green, short-wavelength autofluorescence (420–530 nm); blue, long-wavelength autofluorescence (530–650 nm). Scale bars: A, E, 500 μm; B, F, 100 μm.